

2412 **Chapter 9**
2413 **Weak Focusing Synchrotron**

2414 **Abstract** This Chapter introduces to the weak focusing synchrotron, and to the the-
2415 oretical material needed for the simulation exercises. It begins with a brief reminder
2416 of the historical context, and continues with beam optics and acceleration techniques
2417 which the weak synchrotron principle and methods lean on. Regarding the latter, it
2418 relies on basic charged particle optics and acceleration concepts introduced in the
2419 previous Chapters, and further addresses the following aspects:

- 2420 - fixed closed orbit,
- 2421 - periodic structure,
- 2422 - periodic motion stability,
- 2423 - optical functions,
- 2424 - synchrotron motion,
- 2425 - depolarizing resonances.

2426 The simulation of weak synchrotrons only require a very limited number of optical
2427 elements; actually two are enough: DIPOLE or BEND to simulate combined function
2428 dipoles, and DRIFT to simulate straight section. A third one CAVITE, is required
2429 for acceleration. Particle monitoring requires keywords introduced in the previous
2430 Chapters, including FAISCEAU, FAISTORE, possibly PICKUPS, and some others.
2431 Spin motion computation and monitoring resort to SPNTRK, SPNPRT, FAISTORE.
2432 Optics matching and optimization use FIT[2]. SYSTEM again is used to shorten the
2433 input data files.

2434 **Notations used in the Text**

$B; \mathbf{B}, B_{x,y,s}$	field value; field vector, its components in the moving frame
$B\rho = p/q; B\rho_0$	particle rigidity; reference rigidity
$C; C_0$	orbit length, $C = 2\pi R + \left[\begin{array}{l} \text{straight} \\ \text{sections} \end{array} \right]$; reference, $C_0 = C(p = p_0)$
E	particle energy
EFB	Effective Field Boundary
$f_{\text{rev}}, f_{\text{rf}}$	revolution and accelerating voltage frequencies
h	RF harmonic number, $h = f_{\text{rf}}/f_{\text{rev}}$
$m; m_0; M$	mass, $m = \gamma m_0$; rest mass; in units of MeV/c^2
$n = \frac{\rho}{B} \frac{dB}{d\rho}$	focusing index
$\mathbf{p}; p; p_0$	momentum vector; its modulus; reference
P_i, P_f	polarization, initial, final
q	particle charge
r, R	orbital radius; average radius, $R = C/2\pi$
s	path variable
v	particle velocity
$V(t); \hat{V}$	oscillating voltage; its peak value
x, x', y, y'	horizontal and vertical coordinates in the moving frame
α	momentum compaction, or trajectory deviation
$\beta = v/c; \beta_0; \beta_s$	normalized particle velocity; reference; synchronous
β_u	betatron functions ($u : x, y, Y, Z$)
$\gamma = E/m_0$	Lorentz relativistic factor
$\Delta p, \delta p$	momentum offset
ε	wedge angle
ε_u	Courant-Snyder invariant ($u : x, r, y, l, Y, Z, s$, etc.)
ϵ_R	strength of a depolarizing resonance
μ_u	betatron phase advance, $\mu_u = \int_{\text{period}} ds/\beta_u(s)$ ($u : x, y, Y, Z$)
ν_u	wave number, radial, vertical, synchrotron ($u : x, y, Y, Z, l$)
ρ	curvature radius
$\phi; \phi_s$	particle phase at voltage gap; synchronous phase
ϕ_u	betatron phase advance, $\phi_u = \int ds/\beta_u$ ($u : x, y, Y, \text{or } Z$)
φ	spin angle to the vertical axis

2436 **Introduction**

2437 The synchrotron is an outcome of the mid-1940s longitudinal phase focusing syn-
 2438 chronous acceleration concept [1, 2]. In its early version, transverse beam stability
 2439 in the synchrotron during the thousands of turns that the acceleration lasts was based
 2440 on the technique known at the time: weak focusing, as in the cyclotron and in the be-
 2441 tatron. An existing betatron was used to first demonstrate phase-stable synchronous

2442 acceleration with slow variation of the magnetic field, on a fixed orbit, in 1946 [3],
2443 - closely following the demonstration of the principle of phase focusing using a
2444 fixed-field cyclotron [4].

2445 Phase focusing states that stability of the longitudinal motion, longitudinal focus-
2446 ing, is obtained if particles in a bunch, which have a natural energy spread, arrive
2447 at the accelerating gap in the vicinity of a proper phase of the oscillating voltage,
2448 the synchronous phase; if this condition is fulfilled the bunch stays together, in the
2449 vicinity of the latter, during acceleration. Synchrotrons operate in general in a non-
2450 isochronous regime: the revolution period changes with energy; as a consequence,
2451 in order to maintain an accelerated bunch on the synchronous phase, the RF voltage
2452 frequency, which satisfies $f_{rf} = h f_{rev}$, has to change continuously from injection to
2453 top energy. The reference orbit in a synchrotron is maintained at constant radius by
2454 ramping the guiding field in the main dipoles in synchronism with the acceleration,
2455 as in the betatron [5].

2456 The synchrotron concept allowed the highest energy reach by particle accelerators
2457 at the time, it led to the construction of a series of proton rings with increasing energy:
2458 1 GeV at Birmingham (1953), 3.3 GeV at the Cosmotron (Brookhaven National
2459 Laboratory, 1953), 6.2 GeV at the Bevatron (Berkeley, 1954), 10 GeV at the Synchro-
2460 Phasotron (JINR, Dubna, 1957, operated until 2003), and a few additional ones in
2461 the late 1950s well into the era of the concept which would essentially dethrone the
2462 weak focusing method and its quite bulky rings of magnets which were a practical
2463 limit to further increase in energy¹: the strong focusing synchrotron (the object of
2464 Chapter 10). The general layout of these first weak focusing synchrotrons included
2465 straight sections (often 4, Fig. 9.1), which allowed insertion of injection (Fig. 9.1)
2466 and extraction systems, accelerating cavities, orbit correction and beam monitoring
2467 equipment.

2468 The next decades following the invention of the synchrotron saw applications in
2469 many fields of science including fixed-target nuclear physics for particle discovery,
2470 material science, medicine, industry. Its technological simplicity still makes it an
2471 appropriate technology today in low energy beam application when relatively low
2472 beam current is not a concern, as in the hadrontherapy application (Fig. 9.3) [9]: it
2473 essentially requires a single type of a simple dipole magnet, an accelerating gap, some
2474 command-control instrumentation, whereas it procures greater beam manipulation
2475 flexibilities compared to (synchro-)cyclotrons.

¹ The story has it that it is possible to ride a bicycle in the vacuum chamber of Dubna's Synchro-Phasotron.

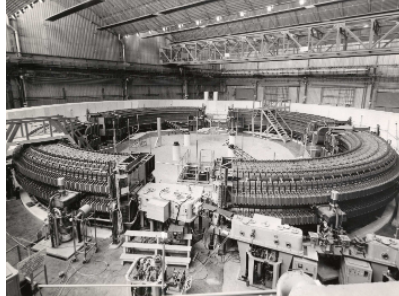


Fig. 9.1 Saturne I at Saclay [6], a 3 GeV, 4-period, 68.9 m circumference, weak focusing synchrotron, constructed in 1956-58. The injection line can be seen in the foreground, injection is from a 3.6 MeV Van de Graaff (not visible)

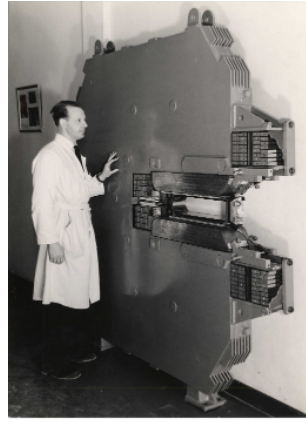


Fig. 9.2 A slice of Saturne I dipole [7]. The slight gap tapering is hardly visible (increasing outward), it determines the weak index condition $0 < n < 1$

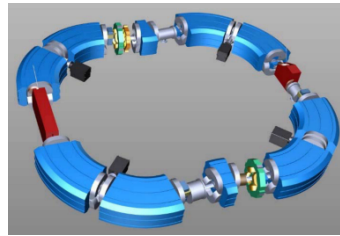
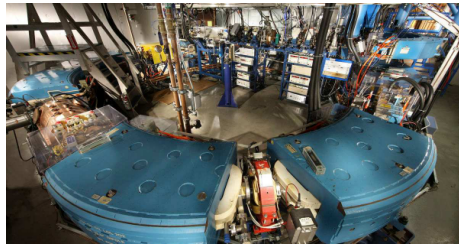


Fig. 9.3 Left: Loma Linda University medical synchrotron. Right: a recent design of a zero-gradient wedge focusing synchrotron for hadrontherapy application [9]

2476 9.1 Basic Concepts and Formulæ

2477 The synchrotron is based on two key principles. On the one hand, a slowly varying
2478 magnetic field to maintain a constant orbit during acceleration,

$$B(t) \times \rho = p(t)/q, \quad \rho = \text{constant}, \quad (9.1)$$

2479 with $p(t)$ the particle momentum and ρ the bending radius in the dipoles. On the other
2480 hand, on synchronous acceleration for longitudinal phase stability. In a regime where
2481 the velocity change with energy cannot be ignored (non-ultrarelativistic particles),
2482 the latter requires a modulation of the accelerating voltage frequency so to satisfy

$$f_{RF}(t) = hf_{rev}(t) \quad (9.2)$$

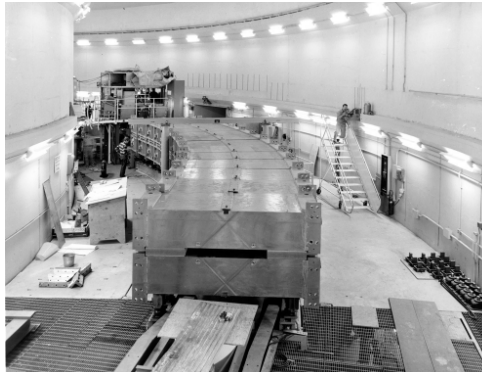
2483 Synchronism between accelerating voltage oscillation and the revolution motion
 2484 keeps the bunch on the synchronous phase at traversal of the accelerating gaps.
 2485 Synchronous acceleration is technologically simpler in the case of electrons, as
 2486 frequency modulation is unnecessary beyond a few MeV; for instance, from $v/c =$
 2487 0.9987 at 10 MeV to $v/c \rightarrow 1$ the relative change in revolution frequency amounts
 2488 to $\delta f_{\text{rev}}/f_{\text{rev}} = \delta\beta/\beta < 0.0013$.

2489 These are two major evolutions compared to the cyclotron, where, instead, the
 2490 magnetic field is fixed - the reference orbit spirals out, and, by virtue of the isochro-
 2491 nism of the orbits, the oscillating voltage frequency is fixed as well.

2492 A fixed orbit reduces the radial extent of individual guiding magnets, allowing a
 2493 ring structure comprised of a circular string of dipoles. For the sake of comparison:
 2494 a synchrocyclotron instead uses a single, massive dipole; increased energy requires
 2495 increased radial extent of the magnet to allow for the greater bending field integral
 2496 (i.e., $\oint B dl = 2\pi R_{\text{max}} \hat{B} = p_{\text{max}}/q$), thus a volume of iron increasing more than
 2497 quadratically with bunch rigidity.

2498 One or the other of the weak index ($-1 < k < 0$, Sect. 4.2.2) and/or wedge
 2499 focusing (Sect. 18.3.1) are used in weak focusing synchrotrons. Transverse stability
 2500 was based on the latter at Argonne ZGS (Zero-Gradient Synchrotron: the main
 2501 magnet had no field index), a 12 GeV, 8-dipole, 4-period ring, operated over 1964-
 2502 1979 (Fig. 9.4). ZGS was the first synchrotron to accelerate polarized proton beams,
 2503 from July 1973 on [8], weak focusing resulted in weak depolarizing resonances, an
 2504 advantage in that matter.

Fig. 9.4 The ZGS at Ar-
 gonne during construction. A
 12 GeV, 8-dipole, 4-period,
 172 m circumference, wedge
 focusing synchrotron. The
 two persons inside and outside
 the ring, in the background,
 give an idea of the size of the
 magnets



2505 Due to the necessary ramping of the field in order to maintain a constant orbit,
 2506 the synchrotron is a pulsed accelerator, the acceleration is cycled, from injection to
 2507 top energy, repeatedly. The repetition rate of the acceleration cyclic depends on the
 2508 type of power supply. If the ramping uses a constant electromotive force ($E=V+ZI$
 2509 is constant), then

$$B(t) \propto (1 - e^{-t/\tau}) = 1 - \left[1 - \left(\frac{t}{\tau}\right) + \left(\frac{t}{\tau}\right)^2 - \dots \right] \approx \frac{t}{\tau} \quad (9.3)$$

2510 essentially linear. In that case $\dot{B} = dB/dt$ does not exceed a few Tesla/second, thus
 2511 the repetition rate of the acceleration cycle is of the order of a Hertz. If instead the
 2512 magnet winding is part of a resonant circuit the field law has the form

$$B(t) = B_0 + \frac{\hat{B}}{2}(1 - \cos \omega t) \quad (9.4)$$

2513 so that, in the interval of half a voltage repetition period (*i.e.*, $t : 0 \rightarrow \pi/\omega$), the
 2514 field increases from an injection threshold value to a maximum value at highest
 2515 rigidity, $B(t) : B_0 \rightarrow B_0 + \hat{B}$. The latter determines the highest achievable energy:
 2516 $\hat{E} = pc/\beta = q\hat{B}\rho c/\beta$. The repetition rate with resonant magnet cycling can reach
 2517 a few tens of Hertz, a species known as “rapid-cycling” synchrotrons. In both cases
 2518 anyway B imposes its law and the other quantities comprising the acceleration cycle
 2519 (RF frequency in particular) will follow B(t).

2520 For the sake of comparison: in a synchrocyclotron the field is constant, thus
 2521 acceleration can be cycled as fast as the swing of the voltage frequency allows
 2522 (hundreds of Hz are common practice); assume a conservative 10 kVolts per turn,
 2523 thus of the order of 10,000 turns to 100 MeV, with velocity $0.046 < v/c < 0.43$
 2524 from 1 to 100 MeV, proton. Take $v \approx 0.5c$ to make it simple, an orbit circumference
 2525 below 30 meter, thus the acceleration takes of the order of $10^4 \times C/0.5c \approx \text{ms}$ range,
 2526 potentially a repetition rate in kHz range, more than an order of magnitude beyond
 2527 the reach of a rapid-cycling pulsed synchrotron.

2528 9.1.1 Periodic Stability

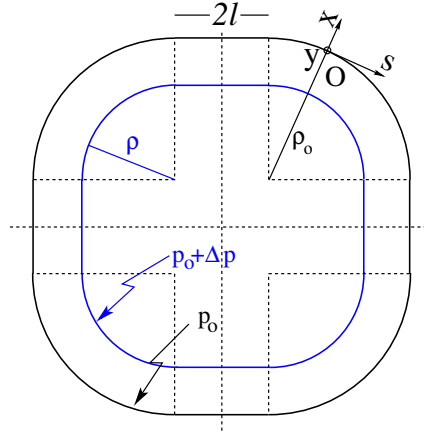
2529 This section introduces the various components of the transverse focusing and the
 2530 conditions for periodic stability in a weak focusing synchrotron. It builds on material
 2531 introduced in Chap. 4, Classical Cyclotron, and on Ref. [13].

2532 9.1.1.1 Closed orbit

2533 The concept is found in the betatron, which accelerates particles on a constant orbit
 2534 (Chap. 7). The closed orbit is fixed, and maintained during acceleration by ensuring
 2535 that the relationship Eq. 9.1 is satisfied. In a perfect ring, the closed orbit is along an
 2536 arc in the bending magnets and straight along the drifts, Fig. 9.5.

2537 Particle motion is defined in a moving frame (O;s,x,y) whose origin coincides
 2538 with the location of an ideal particle following the reference orbit. The moving frame
 2539 s axis is tangent to the reference orbit, its transverse horizontal axis x is normal to
 2540 the s axis, its vertical axis y is normal to the (s, x) plane (Fig. 4.8, Sect. 4.2.2).

Fig. 9.5 A $2\pi/4$ axially symmetric structure with four drift spaces. Orbit length on reference momentum p_0 is $C = 2\pi\rho_0 + 8l$. $(O;s,x,y)$ is the moving frame, along the reference orbit. The orbit for momentum $p = p_0 + \Delta p$ ($\Delta p < 0$, here) is at constant distance $\Delta x = \frac{\rho_0}{1-n} \frac{\Delta p}{p_0} = \frac{R}{(1+k)(1-n)} \frac{\Delta p}{p_0}$ from the reference orbit



2541 **9.1.1.2 Transverse Focusing**

2542 Radial motion stability around a reference closed orbit in an axially symmetric dipole
 2543 field requires a field index (Sect. 4.2.2),

$$n = -\frac{\rho_0}{B_0} \left. \frac{\partial B_y}{\partial \rho} \right|_{x=0, y=0} \quad (9.5)$$

2544 a quantity evaluated on the reference arc in the dipoles, satisfying the weak focusing
 2545 condition

$$0 < n < 1 \quad (9.6)$$

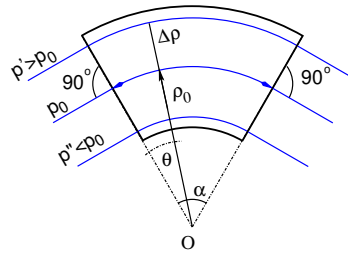
2546 This condition can be obtained with a tapered gap (Fig. 9.2) causing the magnetic
 2547 field to decrease slowly with radius. Note the sign convention here, the cyclotron
 2548 uses the opposite sign (Eq. 4.10). This condition holds regardless of the presence of
 2549 drifts or not. Adding drift spaces between the dipoles, the reference orbit is comprised
 2550 of arcs of radius ρ_0 in the magnets, and straight segments along the drift spaces that
 2551 connect these arcs. This requires defining two radii, namely,

- 2552 (i) the magnet curvature radius ρ_0 ,
- 2553 (ii) an average radius $R = C/2\pi = \rho_0 + Nl/\pi$ (with C the length of the reference
 2554 closed orbit and $2l$ the drift length) (Fig. 9.5) which also writes

$$R = \rho_0(1 + k), \quad k = \frac{Nl}{\pi\rho_0} \quad (9.7)$$

2555 Adding drift spaces decreases the average focusing around the ring.

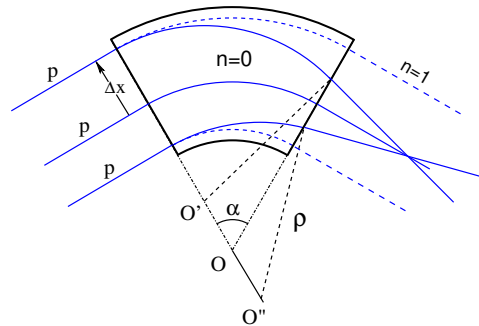
Fig. 9.6 In a sector dipole with radial index $n \neq 0$, closed orbits follow arcs of constant B . A closed orbit at $p_0 + \Delta p$ follows an arc of radius $\rho_0 + \Delta\rho$, $\Delta\rho = \Delta p / (1 + n)qB_0$



2556 *Geometrical focusing*

2557 The limit $n \rightarrow 1$ of the transverse motion stability domain corresponds to a cancel-
 2558 lation of the geometrical focusing (Fig. 9.7): in a constant field dipole (radial field
 2559 index $n=0$) the longer (respectively shorter) path in the magnetic field for parallel
 2560 trajectories entering the magnet at greater (respectively smaller) radius result in
 2561 convergence. This effect is cancelled, *i.e.*, the deviation is the same whatever the
 2562 entrance radius, if the curvature center is made independent of the entrance radius:
 2563 $OO' = 0, O''O = 0$. This occurs if trajectories at an outer (inner) radius experience a
 2564 smaller (greater) field such as to satisfy $BL = B\rho \alpha = C^{st}$. Differentiating $B\rho = C^{st}$
 gives $\frac{\Delta B}{B} + \frac{\Delta\rho}{\rho} = 0$, with $\Delta\rho = \Delta x$, so yielding $n = -\frac{\rho_0}{B_0} \frac{\Delta B}{\Delta x} = 1$. The focal distance

Fig. 9.7 Geometrical focusing: in a sector dipole with focusing index $n = 0$, parallel incoming rays of equal momenta experience the same curvature radius ρ , they exit converging, as a result of the longer path of outer trajectories in the field, compared to inner ones. An index value $n=1$ cancels that effect: rays exit parallel



2565 associated with the curvature is (Eq. 4.12 with $R = \rho_0$) $f = \frac{\rho_0^2}{L}$. Optical drawbacks
 2566 of the weak focusing method include the weakness of the focusing and the absence
 2567 of independent radial and axial focusing.
 2568

2569 *Wedge Focusing*

2570 Entrance and exit wedge angles may be used to ensure transverse focusing: opening
 2571 the magnetic sector increases the horizontal focusing (and decreases the vertical

2572 focusing); closing the magnetic sector has the reverse effect (Sect. 18.3.1). In a point
 2573 transform approximation, at the wedge the trajectory undergoes a local deviation
 2574 proportional to the distance to the optical axis, namely,

$$\Delta x' = \frac{\tan \varepsilon}{\rho_0} \Delta x, \quad \Delta y' = -\frac{\tan(\varepsilon - \psi)}{\rho_0} \Delta y \quad (9.8)$$

2575 ψ is a correction for the fringe field extent (Eq. 18.20), an effect on the vertical
 2576 focusing of the first order in the coordinates (it is a second order effect horizontally).

2577 Profiling the magnet gap in order to adjust the focal distance complicates the
 2578 magnet; a parallel gap, $n = 0$, makes it simpler, for that reason edge focusing
 2579 may be preferred. Wedge vertical focusing in the ZGS ($\varepsilon > 0$) was at the expense
 2580 of horizontal geometrical focusing (Fig. 9.6). This was an advantage though for the
 2581 acceleration of polarized beams, as radial field components (which are responsible for
 2582 depolarization) were only met at the EFBs of the eight main dipoles [8]. Preserving
 2583 beam polarization at high energy required tight control of the tunes, and this was
 2584 achieved by, in addition, pole face windings at the ends of the dipoles [10, 11];
 2585 these coils were pulsed to control the amplitude detuning, resulting in a control
 2586 of the tunes at 0.01 level; they also compensated eddy current induced sextupole
 2587 perturbations which affected the vertical tune.

2588 9.1.1.3 Periodic stability, betatron motion

2589 The first order differential equations of motion in the moving frame (Fig. 9.5) derive
 2590 from the Lorentz equation [13]

$$\frac{d\mathbf{m}\mathbf{v}}{dt} = q\mathbf{v} \times \mathbf{B} \Rightarrow m \frac{d}{dt} \begin{pmatrix} \frac{ds}{dt} \mathbf{s} \\ \frac{dx}{dt} \mathbf{x} \\ \frac{dy}{dt} \mathbf{y} \end{pmatrix} = q \begin{pmatrix} (\frac{dx}{dt} B_y - \frac{dy}{dt} B_x) \mathbf{s} \\ -\frac{ds}{dt} B_y \mathbf{x} \\ \frac{ds}{dt} B_x \mathbf{y} \end{pmatrix} \quad (9.9)$$

2591 Introduce the field index $n = -\frac{\rho_0}{B_0} \frac{\partial B_y}{\partial x}$ evaluated on the reference orbit, with $B_0 =$
 2592 $B_y(\rho_0, y = 0)$; assume transverse stability: $0 < n < 1$. Taylor expansion of the field
 2593 components in the moving frame write

$$B_y(\rho) = B_y(\rho_0) + x \left. \frac{\partial B_y}{\partial x} \right|_{\rho_0} + O(x^2) \approx B_y(\rho_0) - n \frac{B_y}{\rho_0} \Big|_{\rho_0} x = B_0 \left(1 - n \frac{x}{\rho_0}\right)$$

$$B_x(0 + y) = \underbrace{B_x(0)}_{=0} + y \underbrace{\left. \frac{\partial B_x}{\partial y} \right|_{\rho_0}}_{=-\frac{\partial B_y}{\partial x}} + (\text{higher order in } y) \approx -n \frac{B_0}{\rho_0} y \quad (9.10)$$

2594 Introduce in addition $ds \approx v dt$, Eqs. 9.9, 9.10 lead to the differential equations of
 2595 motion in a dipole field

$$\frac{d^2x}{ds^2} + \frac{1-n}{\rho_0^2}x = 0, \quad \frac{d^2y}{ds^2} + \frac{n}{\rho_0^2}y = 0 \quad (9.11)$$

2596 It results that, in an S-periodic structure comprised of dipoles, wedges and drift
 2597 spaces, the differential equation of motion takes the general form of Hill's equation,
 2598 a second order differential equation with periodic coefficient, namely (with u standing
 2599 for x or y),

$$\begin{cases} \frac{d^2u}{ds^2} + K_u(s)u = 0 \\ K_u(s+S) = K_u(s) \end{cases} \quad \text{with} \quad \begin{cases} \text{in dipoles : } \begin{cases} K_x = (1-n)/\rho_0^2 \\ K_y = n/\rho_0^2 \end{cases} \\ \text{at a wedge : } K_x = \pm(\tan \varepsilon)/\rho_0 \\ \text{in drift spaces : } K_x = K_y = 0 \end{cases} \quad (9.12)$$

2600 $K_u(s)$ is S-periodic, $S = 2\pi R/N$ ($S = C/4$, for instance, in the 4-periodic ring
 2601 Saturne 1 (Figs. 9.1, 9.5)). G. Floquet has established [12] that the two independent
 2602 solutions of Hill's second order differential equation have the form [13]

$$\begin{cases} u_1(s) = \sqrt{\beta_u(s)} e^{i \int_0^s \frac{ds}{\beta_u(s)}} \\ du_1(s)/ds = \frac{i - \alpha_u(s)}{\beta_u(s)} u_1(s) \end{cases} \quad \text{and} \quad \begin{cases} u_2(s) = u_1^*(s) \\ du_2(s)/ds = du_1^*(s)/ds \end{cases} \quad (9.13)$$

2603 wherein $\beta_u(s)$ and $\alpha_u(s) = -\beta'_u(s)/2$ are S-periodic functions, from what it results
 2604 that

$$u_{\frac{1}{2}}(s+S) = u_{\frac{1}{2}}(s) e^{\pm i\mu_u} \quad (9.14)$$

2605 wherein

$$\mu_u = \int_{s_0}^{s_0+S} \frac{ds}{\beta_u(s)} \quad (9.15)$$

2606 is the betatron phase advance over a period. A real solution of Hill's equation is
 2607 the linear combination $A u_1(s) + A^* u_2^*(s)$. Take A of the form $A = \frac{1}{2} \sqrt{\varepsilon_u/\pi} e^{i\phi}$
 2608 (the introduction of the constant multiplicative factor $\sqrt{\varepsilon_u/\pi}$ is justified below), the
 2609 general solution of Eq. 9.12 then takes the form (noting $(*)' = d(*)/ds$)

$$\begin{cases} u(s) = \sqrt{\beta_u(s)\varepsilon_u/\pi} \cos\left(\int \frac{ds}{\beta_u} + \phi\right) \\ u'(s) = -\sqrt{\frac{\varepsilon_u/\pi}{\beta_u(s)}} \sin\left(\int \frac{ds}{\beta_u} + \phi\right) + \alpha_u(s) \cos\left(\int \frac{ds}{\beta_u} + \phi\right) \end{cases} \quad (9.16)$$

2610 An invariant of the motion is

$$\frac{1}{\beta_u(s)} [u^2 + (\alpha_u(s)u + \beta_u(s)u')^2] = \frac{\varepsilon_u}{\pi} \quad (9.17)$$

2611 known as the Courant-Snyder invariant. At a given azimuth s of the periodic structure the observed turn-by-turn motion lies on that ellipse (Fig. 9.8). The form and
 2612 inclination of the ellipse depend on the observation azimuth s via the respective local
 2613 values of $\alpha_u(s)$ and $\beta_u(s)$, but its surface ε_u is invariant. Motion along the ellipse
 2614 is clockwise, as can be figured from Eq. 9.16 considering an observation azimuth s
 2615 where the ellipse is upright, $\alpha_u(s) = 0$.
 2616

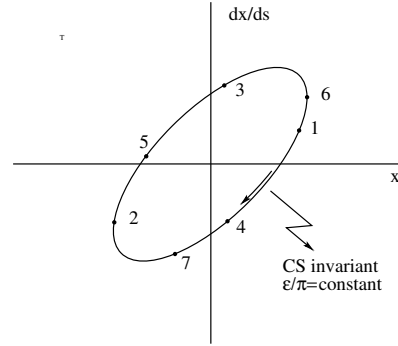


Fig. 9.8 Courant-Snyder invariant and turn-by-turn harmonic motion along the invariant, observed at some azimuth s . The form of the ellipse depends on the observation azimuth s but its surface ε_u is invariant

2617 If the ring is comprised of N periods, the phase advance over a turn (from one
 2618 location to the next on the ellipse in Fig. 9.8) is

$$\int_{s_0}^{s_0+NS} \frac{ds}{\beta_u(s)} = N \int_{s_0}^{s_0+S} \frac{ds}{\beta_u(s)} = N\mu_u \quad (9.18)$$

2619 *Weak focusing approximation*

2620 In the case of a cylindrically symmetric structure, a sinusoidal motion is the exact
 2621 solution of the first order differential equations of motion (Eqs. 4.14, 4.15, Classical
 2622 Cyclotron Chapter). In that case the latter have a constant (s -independent) coefficient,
 2623 $K_x = (1 - n)/R_0^2$ and $K_y = n/R_0^2$, respectively. Adding drift spaces results in Hill's
 2624 differential equation with periodic coefficient $K(s + S) = K(s)$ (Eq. 9.12), and in a
 2625 pseudo harmonic solution (Eq. 9.16). Due to the weak focusing the beam envelope
 2626 (Eq. 9.24) is only weakly modulated, thus so is $\beta_u(s)$. In a practical manner, the
 2627 modulation of $\beta_u(s)$ does not exceed a few percent, this justifies introducing the
 2628 average value $\bar{\beta}_u$ to approximate the phase advance by

$$\int_0^s \frac{ds}{\beta_u(s)} \approx \frac{s}{\bar{\beta}_u} = \nu_u \frac{s}{R} \quad (9.19)$$

2629 The right equality is obtained by applying this approximation to the the phase advance
 2630 per period (Eq. 9.15), namely $\mu_u = \int_{s_0}^{s_0+S} \frac{ds}{\beta_u(s)} \approx S/\bar{\beta}_u$, and introducing the wave

2631 number of the N-period optical structure

$$v_u = \frac{N\mu_u}{2\pi} = \frac{\text{phase advance over a turn}}{2\pi} \quad (9.20)$$

2632 so that

$$\overline{\beta_u} = \frac{R}{v_u} \quad (9.21)$$

2633 Substituting in Eq. 9.16 results in the approximate solution

$$\begin{cases} u(s) \approx \sqrt{\beta_u(s)\varepsilon_u/\pi} \cos\left(v_u \frac{s}{R} + \phi\right) \\ u'(s) = -\sqrt{\frac{\varepsilon_u/\pi}{\beta_u(s)}} \sin\left(v_u \frac{s}{R} + \phi\right) + \alpha_u(s) \cos\left(v_u \frac{s}{R} + \phi\right) \end{cases} \quad (9.22)$$

2634 In this approximation, the differential equations of motion (Eq. 9.12) can be expressed
2635 under the form

$$\frac{d^2x}{ds^2} + \frac{v_x^2}{R^2}x = 0, \quad \frac{d^2y}{ds^2} + \frac{v_y^2}{R^2}y = 0 \quad (9.23)$$

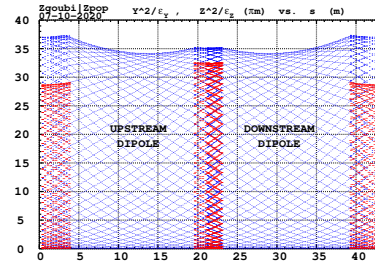
2636 *Beam envelopes*

2637 The beam envelope $\hat{u}(s)$ (with u standing for x or y) is determined by the particle of
2638 maximum invariant ε_u/π , it is given by

$$\pm \hat{u}(s) = \pm \sqrt{\beta_u(s)\varepsilon_u/\pi} \quad (9.24)$$

As $\beta_u(s)$ is S-periodic, so is the envelope, $\hat{u}(s+S) = \hat{u}(s)$. In a cell with symmetries

Fig. 9.9 ***** replace
par envelope in saturne1
***** Beam envelope
along Saturne I four cells,
generated by a single particle
over many turns. The extreme
excursion at any azimuth
 s tangents the envelope.
Envelopes along a cell feature
central symmetry, as does the
cell



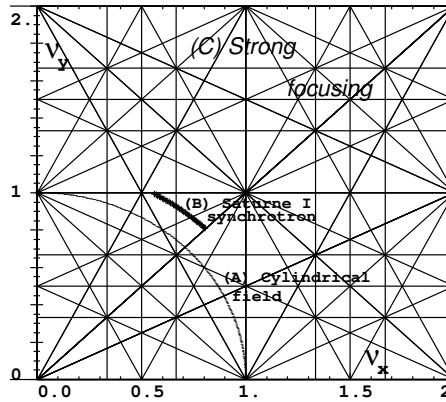
2639 (for instance symmetry with respect to the center of the cell), the envelope features
2640 the same symmetries. Envelope extrema are at azimuth s where $\beta_u(s)$ is minimum,
2641 or maximum, *i.e.*, where $\alpha_u = 0$ as $\beta'_u = -2\alpha_u$. This is illustrated in Fig. 9.9. No
2642 particular hypothesis regarding the amplitude of the motion is required here, it does
2643

2644 not have to be paraxial and can be arbitrarily large (as long as transverse stability
2645 still holds).

2646 *Working point*

2647 The “working point” of the synchrotron is the wave number couple (ν_x, ν_y) at which
2648 the accelerator is operated, it fully characterizes the focusing. In a structure with
2649 cylindrical symmetry (cf. Eq. 4.16) $\nu_x = \sqrt{1-n}$ and $\nu_y = \sqrt{n}$ so that $\nu_x^2 + \nu_y^2 = 1$:
2650 when the radial field index n is changed the working point stays on a circle of radius 1
in the stability diagram (or “tune diagram”, Fig. 9.10). If drift spaces are added, in

Fig. 9.10 Location of the working point in the tune diagram, in case of (A) field with revolution symmetry, on a circle of radius 1; (B) sector field with index + drift spaces, on a circle of radius $(\sqrt{R/\rho_0})$; (C) strong focusing, $(|n| \gg 1)$, in large ν_x, ν_y regions.



2651 a first approximation
2652

$$\nu_x = \sqrt{(1-n)\frac{R}{\rho_0}}, \quad \nu_y = \sqrt{n\frac{R}{\rho_0}}, \quad \nu_x^2 + \nu_y^2 = \frac{R}{\rho_0} \quad (9.25)$$

the working point is located on the circle of radius $\sqrt{R/\rho_0} > 1$. Tunes can not exceed the limits

$$0 < \nu_{x,y} < \sqrt{R/\rho_0}$$

2653 Horizontal and vertical focusing are not independent: if ν_x increases then ν_y de-
2654 creases and reciprocally. This is a lack of flexibility which the advent of strong
2655 focusing will overcome by providing two knobs allowing separate adjustment of the
2656 tunes.

2657 **Off-momentum orbits**

In a dipole with field index $n = -\frac{\rho_0}{B_0} \frac{\partial B_y}{\partial \rho}$, orbits different momenta $p = p_0 + \Delta p$ are concentric (Fig. 9.6), distant (after Eq. 4.18)

$$\Delta x = \frac{\rho_0}{1-n} \frac{\Delta p}{p_0}$$

2658 from the reference orbit. Introduce now the geometrical radius $R = (1+k)\rho_0$ (Eq. 9.7)
2659 to account for the added drifts, this gives

$$\frac{\Delta x}{\Delta p/p_0} \equiv \frac{\Delta R}{\Delta p/p_0} = \frac{R}{(1-n)(1+k)} \quad (9.26)$$

2660 Thus the chromatic dispersion of the orbits, the dispersion function

$$D = \frac{\Delta x}{\Delta p/p_0} = \frac{R}{(1-n)(1+k)}, \quad \text{constant} \quad (9.27)$$

2661 an s -independent quantity: in a structure with axial symmetry, comprising drift
2662 sections (Fig. 9.5) or not (classical and AVF cyclotrons for instance), the ratio
2663 $\frac{\Delta x}{\rho_0 \Delta p/p_0}$ is independent of the azimuth s , the distance of a chromatic orbit to the
2664 reference orbit is constant around the ring.

2665 Given that $n < 1$,

- 2666 - higher momentum orbits, $p > p_0$, have a greater radius,
- 2667 - lower momentum orbits, $p < p_0$, have a smaller radius.

2668 *Chromatic orbit length*

2669 In an axially symmetric structure the difference in closed orbit length $\Delta C = 2\pi\Delta R$
2670 resulting from the difference in momentum arises in the dipoles, as all orbits are
2671 parallel in the drifts (Fig. 9.5). Hence, from Eq. 9.26, the relative closed orbit
2672 lengthening factor, "momentum compaction"

$$\alpha = \frac{\Delta C}{C} \Big/ \frac{\Delta p}{p_0} \equiv \frac{\Delta R}{R} \Big/ \frac{\Delta p}{p_0} = \frac{1}{(1-n)(1+k)} \approx \frac{1}{v_x^2} \quad (9.28)$$

2673 with $k = Nl/\pi\rho_0$ (Eq. 9.7). Note that the relationship $\alpha \approx 1/v_x^2$ between momentum
2674 compaction and horizontal wave number established for a revolution symmetry
2675 structure (Eq. 4.20) still holds when adding drifts.

2676 **9.1.1.4 Longitudinal Motion**

The acceleration of the ideal particle is addressed in this Section. In a synchrotron,
the field B is varied (a function performed by the power supply) concurrently with

the bunch momentum p (a function performed by the accelerating cavity) in such a way that at any time

$$B(t)\rho = p(t)/q$$

If this condition is fulfilled, then at all times during the acceleration cycle the beam is maintained on the design orbit. Given the energies involved, the magnet supply imposes its law and the cavity follows $B(t)$, the best it can. A schematic $B(t)$ law is represented in Fig. 9.11. The accelerating voltage $\hat{V}(t) = \sin \omega_{rf}t$ is maintained

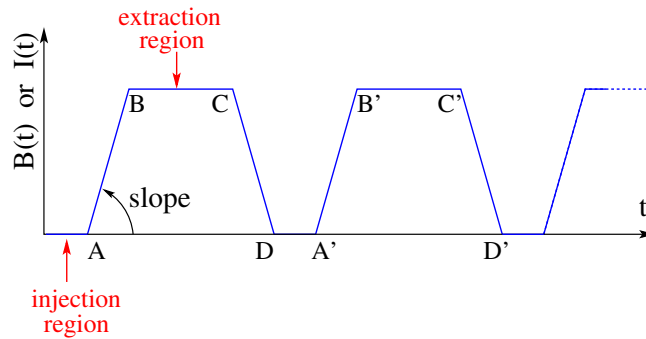


Fig. 9.11 Cycling $B(t)$ in a pulsed synchrotron. Ignoring saturation, $B(t)$ is proportional to the magnet power supply current $I(t)$. Bunch injection occurs at low field, in the region of A, extraction occurs at top energy, on the high field plateau. (AB): field ramp up (acceleration); (BC): flat top (includes beam extraction period); (CD): field ramp down; (DA'): thermal relaxation. (AA'): repetition period; $(1/AA')$: repetition rate; *slope*: ramp velocity $\dot{B} = dB/dt$ (Tesla/s).

in synchronism with the revolution motion, thus its angular frequency ω_{rf} follows hf_{rev} ,

$$\omega_{rf} = h\omega_{rev} = h \frac{c}{R} \frac{B(t)}{\sqrt{\left(\frac{m_0}{q\rho}\right)^2 + B^2(t)}}$$

2677 *Energy gain*

2678 The variation of the particle energy over a turn amounts to the work of the force
2679 $F = dp/dt$ on the charge at the cavity, namely

$$\Delta W = F \times 2\pi R = 2\pi q R \rho \dot{B} \tag{9.29}$$

Over most of the acceleration cycle in a slow-cycling synchrotron \dot{B} is usually constant (Eq. 9.3), thus so is ΔW . At Saturne I for instance (the parameters of the synchrotron can be found in Tab. 9.1, Exercise 9.1)

$$\frac{\Delta W}{q} = 2\pi R \rho \dot{B} = 68.9 \times 8.42 \times 1.8 = 1044 \text{ volts}$$

The field ramp lasts

$$\Delta t = (B_{\max} - B_{\min}) / \dot{B} \approx B_{\max} / \dot{B} = 0.8 \text{ s}$$

The number of turns to the top energy ($W_{\max} \approx 3 \text{ GeV}$) is

$$N = \frac{W_{\max}}{\Delta W} = \frac{3 \cdot 10^9 \text{ eV}}{1044 \text{ eV}} \approx 3 \cdot 10^6$$

2680 *Adiabatic damping of the betatron oscillations*

During acceleration, focusing strengths follow the increase of particle rigidity, so to maintain the tunes ν_x and ν_y constant. As a result of the longitudinal acceleration at the cavity though, the longitudinal energy of the particles is modified. This results in a decrease of the amplitude of betatron oscillations (an increase if the cavity is decelerating). The mechanism is sketched in Fig. 9.12: the slope, respectively before (index 1) and after (index 2) the cavity is

$$\frac{dx}{ds} = \frac{m \frac{dx}{dt}}{m \frac{ds}{dt}} = \frac{p_x}{p_s}, \quad \left. \frac{dx}{ds} \right|_2 = \frac{m \frac{dx}{dt}}{m \frac{ds}{dt}} \Big|_2 = \frac{p_{x,2}}{p_{s,2}}$$

Particle mass and velocity are modified at the traversal of the cavity but, as the

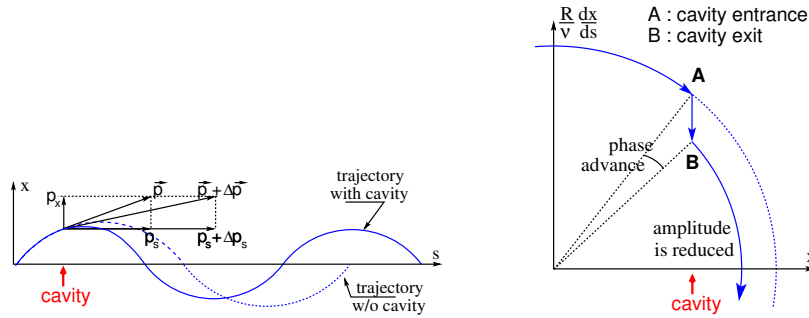


Fig. 9.12 Adiabatic damping of betatron oscillations, here from $x' = p_x/p_s$ before the cavity, to $x'_2 = p_x/(p_s + \Delta p_s)$ after the cavity. In the horizontal phase space, to the right, decrease of $\Delta \left(\frac{dx}{ds} \right)$ if $\frac{dx}{ds} > 0$, increase of $\Delta \left(\frac{dx}{ds} \right)$ if $\frac{dx}{ds} < 0$

force is longitudinal, $dp_x/dt = 0$ thus $p'_x = p_x$, the increase in momentum is purely longitudinal, $p'_s = p_s + \Delta p$. Thus

$$\left. \frac{dx}{ds} \right|_2 = \frac{p_x}{p_s + \Delta p} \approx \frac{p_x}{p_s} \left(1 - \frac{\Delta p}{p_s}\right)$$

and as a consequence the slope dx/ds varies across the cavity,

$$\Delta \left(\frac{dx}{ds} \right) = \left. \frac{dx}{ds} \right|_2 - \frac{dx}{ds} = - \frac{dx}{ds} \frac{\Delta p_s}{p_s}$$

2681 The slope varies in proportion to the slope, with opposite sign if $\Delta p/p > 0$ (accel-
2682 eration) thus a decrease of the slope. This variation has two consequences on the
2683 betatron oscillation (Fig. 9.12):

- 2684 - a change of the betatron phase,
- 2685 - a modification of the betatron amplitude.

2686 *In matrix form*

2687 Coordinate transport through the cavity writes $\begin{cases} x_2 = x \\ x'_2 \approx \frac{p_x}{p_s} \left(1 - \frac{dp}{p}\right) = x' \left(1 - \frac{dp}{p}\right) \end{cases}$,
2688 hence the transfer matrix of the cavity,

$$[C] = \begin{bmatrix} 1 & 0 \\ 0 & 1 - \frac{dp}{p} \end{bmatrix} \quad (9.30)$$

2689 its determinant is $1 - dp/p \neq 1$: the system is non-conservative (the surface in phase
2690 space is not conserved). Assume one cavity in the ring and not $[T] \times [C]$ the one-turn
2691 matrix with origin at entrance of the cavity. Its determinant is $\det[T] \times \det[C] =$
2692 $\det[C] = 1 - \frac{dp}{p}$. Over N turns the coordinate transport matrix is $([T][C])^N$, its
2693 determinant is $\left(1 - \frac{dp}{p}\right)^N \approx 1 - N \frac{dp}{p}$. The surface of the longitudinal beam ellipse
2694 is $\varepsilon_l \times \det[T]_{turn} = \varepsilon_{l,0} - \varepsilon_l \frac{dp}{p}$ thus $\frac{d\varepsilon_l}{\varepsilon_l} = -\frac{dp}{p}$, the solution of which is

$$\varepsilon_l \times p = \text{constant}, \quad \text{or} \quad \beta\gamma\varepsilon = \text{constant} \quad (9.31)$$

2695 *Synchrotron motion; the synchronous particle*

2696 By “synchrotron motion”, or “phase oscillations”, it is meant a mechanism that
2697 stabilizes the longitudinal motion of a particle around a synchronous phase, in virtue
2698 of

- 2699 (i) the presence of an accelerating cavity with its frequency indexed on the
2700 revolution time,
- 2701 (ii) with the bunch centroid positioned either on the rising slope of the oscillating
2702 voltage (low energy regime), or on the falling slope (high energy regime).

The synchronous (or “ideal”) particle follows the equilibrium trajectory around
the ring (the reference closed orbit, about which all other particles will undergo a

betatron oscillation) and its velocity satisfies

$$B\rho = \frac{p}{q} = \frac{mv}{p} \rightarrow v = \frac{qB\rho}{m}$$

- 2703 - the revolution time is $T_{rev} = \frac{2\pi R}{v} = \frac{2\pi R}{\beta c} = \frac{2\pi R}{qB\rho/m}$
 - the angular revolution frequency follows the increase of B:

$$\omega_{rev} = \frac{2\pi}{T_{rev}} = \frac{qB\rho}{mR}$$

- 2704 - during the acceleration $B(t)$ increases at a $\frac{dB}{dt} = \dot{B}$ rate normally of the order of a
 2705 Tesla/second.

- in order for the ideal particle to stay on the closed orbit during the acceleration, its changing momentum must at all time satisfy $B(t)\rho = p(t)/q$. This defines $p(t)$ as a function of $B(t)$, and the following B dependence of mass and angular frequency:

$$m(t) = \gamma(t)m_0 = \frac{q\rho}{c} \sqrt{\left(\frac{m_0}{qc\rho}\right)^2 + B(t)^2}$$

$$\omega_{rev}(t) = \frac{c}{R} \frac{B(t)}{\sqrt{\left(\frac{m_0}{qc\rho}\right)^2 + B(t)^2}}$$

- 2706 - the RF voltage frequency $\omega_{RF}(t) = h\omega_{rev}(t)$ follows B(t), this maintains the
 2707 synchronous phase at a fixed value
 2708 - over a turn the gain in energy is $\Delta W = 2\pi qR\rho\dot{B}$, the reference particle experiences
 2709 a voltage $V = \Delta W/q = 2\pi R\rho\dot{B}$.
 2710 Simulation wise, the ramping of the guide field can be assumed to follow a step
 2711 function in correlation with the step increase of particle momentum at the RF cavity.
 2712 In that manner, the synchronous particle is maintained on the design orbit, at radius
 2713 $\rho = p(t)/qB(t)=\text{constant}$ in the guide magnets.

2714 *Phase Stability*

- 2715 The mechanism of phase stability has, first experimented in the synchrocyclotron [14]
 2716 has been introduced in the eponym Chapter (Chap. 8). It is re-visited here accounting
 2717 for specificities of the operation of a synchrotron, such as the constant radius orbit,
 2718 or the concept of transition energy.

Note ϕ_s the RF phase at arrival of the synchronous particle at the aforementioned accelerating cavity, its energy gain is

$$\Delta W = q\hat{V} \sin \phi_s = 2\pi qR\rho\dot{B}$$

The condition $|\sin \phi_s| < 1$ imposes a lower limit to the cavity voltage for acceleration to happen, namely

$$\hat{V} > 2\pi R \rho \hat{B}$$

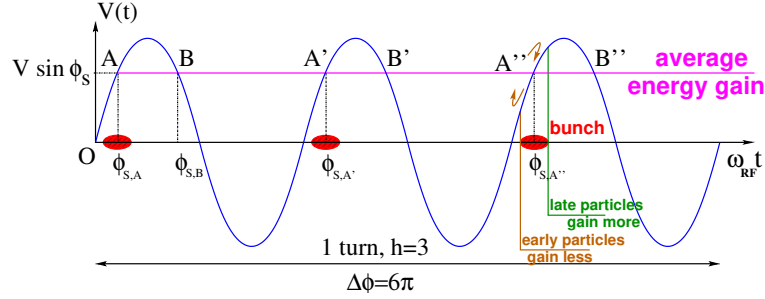


Fig. 9.13 Mechanism of phase stability, “longitudinal focusing”. Below transition ($\gamma < \gamma_{tr}$) phase stability occurs for a synchronous phase taken at either of the $h=3$ stable locations A, A', A'': a particle with higher energy goes around the ring more rapidly than the synchronous particle, it arrives earlier at the voltage gap (at $\phi < \phi_{s,A}$) and experiences a lower voltage; at lower energy the particle is slower, it arrives at the gap later compared to the synchronous particle, at $\phi > \phi_{s,A}$, and experiences a greater voltage; this results overall in a stable oscillatory motion around the synchronous phase. Beyond transition ($\gamma > \gamma_{tr}$) the stable phase is at either of the $h=3$ stable locations B, B', B'': a particle which is less energetic than the synchronous particle arrives earlier, $\phi < \phi_{s,B}$, it experiences a greater voltage, and inversely when it eventually gets more energetic than the synchronous particle

2719 Referring to Fig. 9.13, the synchronous phase can be placed on the left (A A' A'')...
 2720 series in the Figure, or on the right (B B' B'')... series) of the oscillating voltage crest.
 2721 One and only one of these two possibilities, and which one depends on the optical
 2722 lattice and on particle energy, ensures that particles in a bunch remain grouped in the
 2723 vicinity of the synchronous particles. The transition between these two regimes (A
 2724 series or B series) occurs at the transition γ , γ_{tr} , a property of the lattice. If the bunch
 2725 energy is below transition energy, $E_{bunch} < m\gamma_{tr}$, the bunch has to present itself on
 2726 the left of the crest (A series), if the bunch energy is greater than transition energy,
 2727 $E_{bunch} > m\gamma_{tr}$, the bunch has to present itself on the right of the crest (B series).

2728 *Transition energy*

2729 The transition between the two regimes occurs at $\frac{dT_{rev}}{T_{rev}} = 0$. With $T = 2\pi/\omega = C/v$,
 2730 this can be written $\frac{d\omega_{rev}}{\omega_{rev}} = -\frac{dT_{rev}}{T_{rev}} = \frac{dv}{v} - \frac{dC}{C}$. With $\frac{dv}{v} = \frac{1}{\gamma^2} \frac{dp}{p}$ and momentum
 2731 compaction $\alpha = \frac{dC}{C} / \frac{dp}{p}$, (Eq. 9.28), this can be written

$$\frac{d\omega_{\text{rev}}}{\omega_{\text{rev}}} = -\frac{dT_{\text{rev}}}{T_{\text{rev}}} = \left(\frac{1}{\gamma^2} - \alpha\right) \frac{dp}{p} = \eta \frac{dp}{p} \quad (9.32)$$

2732 wherein the phase-slip factor has been introduced,

$$\eta = \overbrace{\frac{1}{\gamma^2}}^{\text{kinematics}} - \underbrace{\alpha}_{\text{lattice}} \quad (9.33)$$

2733 In a weak focusing structure $\alpha \approx 1/v_x^2$ (Eqs. 4.20, 9.28), thus the phase stability
2734 regime is

$$\text{below transition, i.e. } \phi_s < \pi/2, \quad \text{if } \gamma < v_x \quad (9.34)$$

$$\text{above transition, i.e. } \phi_s > \pi/2, \quad \text{if } \gamma > v_x \quad (9.35)$$

$$(9.36)$$

2735 In a weak focusing synchrotron the horizontal tune $\nu_x = \sqrt{(1-n)R/\rho_0}$ (Eq. 9.25)
2736 may be ≥ 1 , and subsequently $\gamma_{\text{tr}} \approx \nu_x \geq 1$ depending on the horizontal tune value.
2737 Saturne I for instance, with $\nu_x \approx 0.7$ (Tab. 9.1), operated above transition energy.

2738 9.1.2 Spin Motion, Depolarizing Resonances

2739 The availability of polarized proton sources allowed the acceleration of polarized
2740 beams to high energy. The possibility was considered from the early times of the
2741 ZGS [15], up to 70% polarization transmission through the synchrotron was fore-
2742 seen, polarization manipulation concepts included harmonic orbit correction, tune
2743 jump at strongest depolarizing resonances (Fig. 9.14). Acceleration of a polarized
2744 proton beam happened for the first time in a synchrotron and to multi-GeV energy in
2745 1973, four years after the ZGS startup. Beams were accelerated up to 17 GeV with
2746 substantial polarization maintained [8]. Experiments were performed to assess the
2747 possibility of polarization transmission in strong focusing synchrotrons, and polar-
2748 ization lifetime in colliders [16]. Acceleration of polarized deuteron was achieved in
2749 the late 1970s, when sources were made available [17].

2750 The field index is essentially zero in the ZGS, transverse focusing is ensured
2751 by wedge angles at the ends of the height dipoles, which is thus the only location
2752 where non-zero horizontal field components are found. The vertical wave number
2753 is small in addition, less than 1. This results in depolarizing resonance strengths
2754 on the weak side, “As we can see from the table, the transition probability [from
2755 spin state $\psi_{1/2}$ to spin state $\psi_{-1/2}$] is reasonably small up to $\gamma = 7.1$ ” [8], i.e.
2756 $G\gamma = 12.73$, $p = 6.6$ GeV/c; the table referred to stipulates a transition probability
2757 $P_{\frac{1}{2}, -\frac{1}{2}} < 0.042$, whereas resonances beyond that energy range feature $P_{\frac{1}{2}, -\frac{1}{2}} > 0.36$.

2758 Beam depolarization up to 6 GeV/c, under the effect of these resonances, is illustrated
 2759 in Fig. 9.14.

2760 In weak focusing synchrotron particles experience radial fields all along the
 2761 bend dipoles as an effect of the radial field index, as they undergo vertical betatron
 2762 oscillations. However these radial field components are weak, and so is there effect
 2763 on spin motion, as long as the particle energy (the γ factor in the spin precession
 2764 equation) is not too high.

Assuming a defect-free ring, the vertical betatron motion excites “intrinsic” spin resonances, located at

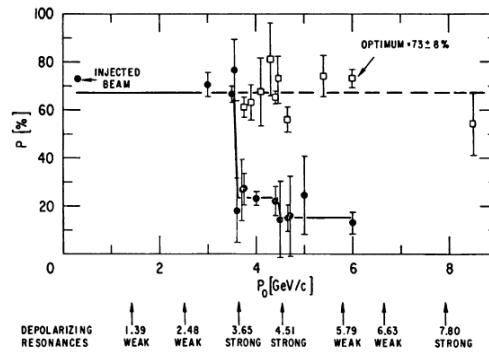
$$G\gamma_R = k P \pm \nu_y$$

with k an integer and P the period of the ring. In the ZGS for instance, $\nu_y \approx 0.8$ (Tab. 9.2), the ring P=4-periodic, thus $G\gamma_R = 4k \pm 0.8$. Strongest resonances are located at

$$G\gamma_R = MP k \pm \nu_y$$

2765 with M the number of cells per superperiod [18, Sec. 3.II]. In the ZGS, M=2 thus strongest resonances occur at $G\gamma_R = 2 \times 4k \pm 0.8$.

Fig. 9.14 Depolarizing intrinsic resonance landscape up to 6 GeV/c at the ZGS (solid circles). Systematic resonances are located at $G\gamma_R = 4 \times \text{integer} \pm \nu_y$, stronger ones at $G\gamma_R = 8 \times \text{integer} \pm \nu_y$. Tune jump was used to preserve polarization when crossing strong resonances (empty circles) [?]



2766 In the presence of vertical orbit defects, non-zero periodic transverse fields are experienced along the closed orbit, they excite “imperfection” depolarizing resonances, located at

$$G\gamma_R = k$$

with k an integer. In the case of systematic defects the periodicity of the orbit is that of the lattice, P, imperfection resonances are located at $G\gamma_R = kP$. Strongest imperfection resonances are located at

$$G\gamma_R = MP k$$

2767 with M the number of cells per superperiod [18, Sec. 3.II]. Crossing a depolarizing
 2768 resonance, during acceleration, causes a loss of polarization given by (Froissart-Stora

2769 formula [19])

$$\frac{P_f}{P_i} = 2e^{-\frac{\pi}{2} \frac{|\epsilon_R|^2}{\alpha}} - 1 \quad (9.37)$$

2770 from a value P_i upstream to an asymptotic value P_f downstream of the resonance.
2771 This assumes an isolated resonance, passed with a crossing speed

$$\alpha = G \frac{d\gamma}{d\theta} = \frac{1}{2\pi} \frac{\Delta E}{M} \quad (9.38)$$

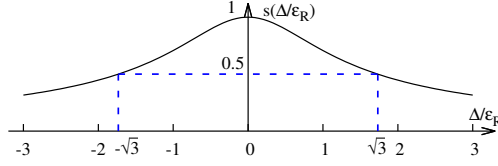
2772 with ΔE the energy gain per turn and M the mass. ϵ_R is the resonance strength.

2773 *Spin precession axis. Resonance width*

2774 Consider the spin vector $\mathbf{S}(\theta) = (S_\eta, S_\xi, S_y)$ of a particle in the laboratory frame,
2775 with θ the orbital angle around the accelerator. Introduce the projection $s(\theta)$ of \mathbf{S}
2776 in the median plane

$$s(\theta) = S_\eta(\theta) + jS_\xi(\theta) \quad (\text{and } S_y^2 = 1 - s^2) \quad (9.39)$$

Fig. 9.15 Modulus of the horizontal spin component. $s = 1/2$ at distance $\Delta = \pm\sqrt{3}\epsilon_R$ from $G\gamma_R$



2777

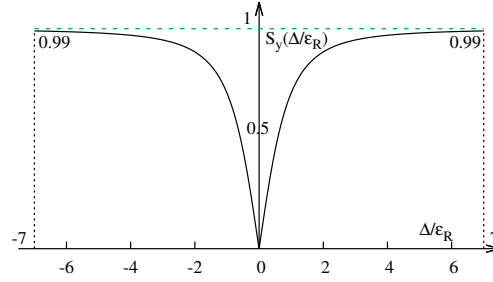
2778 It can be shown that in the case of a stationary solution of the spin motion (*i.e.*,
2779 the spin precession axis) s satisfies [20] (Fig. 9.15)

$$s^2 = \frac{1}{1 + \frac{\Delta^2}{|\epsilon_R|^2}} \quad (9.40)$$

2780 wherein $\Delta = G\gamma - G\gamma_R$ is the distance to the resonance. The resonance width is a
2781 measure of its strength (Fig. 9.16). The quantity of interest is the angle, ϕ , of the
2782 spin precession direction to the vertical axis, given by (Fig. 9.16)

$$\cos \phi(\Delta) \equiv S_y(\Delta) = \sqrt{1 - s^2} = \frac{\Delta/|\epsilon_R|}{\sqrt{1 + \Delta^2/|\epsilon_R|^2}} \quad (9.41)$$

Fig. 9.16 Dependence of polarization on the distance to the resonance. For instance $S_y = 0.99$, 1% depolarization, corresponds to $\Delta = 7|\epsilon_R|$. On the resonance, $\Delta = 0$, the precession axis lies in the median plane, $S_y = 0$



2783 On the resonance, $\Delta = 0$, the spin precession axis lies in the bend plane: $\phi = \pm\pi/2$.
 2784 $S_y = 0.99$ (1% depolarization) corresponds to a distance to the resonance $\Delta = 7|\epsilon_R|$,
 2785 and spin precession axis at an angle $\phi = \text{acos}(0.99) = 8^\circ$ from the vertical.

2786 Conversely,

$$\frac{\Delta^2}{|\epsilon_R|^2} = \frac{S_y^2}{1 - S_y^2} \quad (9.42)$$

The precession axis is common to all spins, S_y is a measure of the polarization along the vertical axis,

$$S_y = \frac{N^+ - N^-}{N^+ + N^-}$$

2787 wherein N^+ and N^- denote the number of particles in spin states $\frac{1}{2}$ and $-\frac{1}{2}$ respectively.
 2788

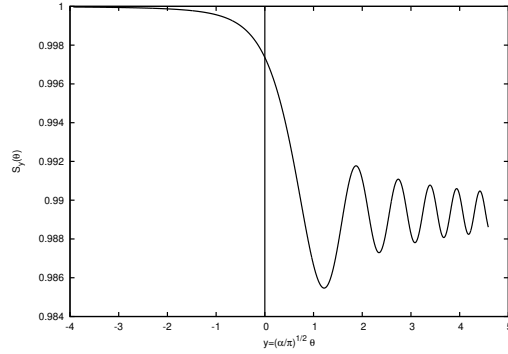
2789 *Spin motion through weak resonances*

Depolarizing resonances are weak up to several GeV in a weak focusing synchrotron, as the radial and/or longitudinal fields, which stem from a small radial field index and from dipole fringe fields, are weak. Spin motion $S_y(\theta)$ through a resonance in that case (*i.e.*, assuming $S_{y,f} \approx S_{y,i}$, with $S_{y,f}$ and $S_{y,i}$ the asymptotic vertical spin component values respectively upstream and downstream of the resonance) can be calculated in terms of the Fresnel integrals

$$C(x) = \int_0^x \cos\left(\frac{\pi}{2}t^2\right) dt, \quad S(x) = \int_0^x \sin\left(\frac{\pi}{2}t^2\right) dt$$

2790 namely, with the origin of the orbital angle taken at the resonance [20] (Fig. 9.17)

Fig. 9.17 Vertical component of spin motion $S_y(\theta)$ through a weak depolarizing resonance (after Eq. 9.43). The vertical bar is at the location of the resonance, which coincides with the origin of the orbital angle



$$\begin{aligned}
 \text{if } \theta < 0 : \left(\frac{S_y(\theta)}{S_{y,i}} \right)^2 &= 1 - \frac{\pi}{\alpha} |\epsilon_R|^2 \left\{ \left[0.5 - C \left(-\theta \sqrt{\frac{\alpha}{\pi}} \right) \right]^2 + \left[0.5 - S \left(-\theta \sqrt{\frac{\alpha}{\pi}} \right) \right]^2 \right\} \\
 \text{if } \theta > 0 : \left(\frac{S_y(\theta)}{S_{y,i}} \right)^2 &= 1 - \frac{\pi}{\alpha} |\epsilon_R|^2 \left\{ \left[0.5 + C \left(\theta \sqrt{\frac{\alpha}{\pi}} \right) \right]^2 + \left[0.5 + S \left(\theta \sqrt{\frac{\alpha}{\pi}} \right) \right]^2 \right\} \quad (9.43)
 \end{aligned}$$

2791 In the asymptotic limit,

$$\frac{S_y(\theta)}{S_{y,i}} \xrightarrow{\theta \rightarrow \infty} 1 - \frac{\pi}{\alpha} |\epsilon_R|^2 \quad (9.44)$$

2792 which identifies with the development of Froissart-Stora formula $P_f/P_i = 2 \exp(-\frac{\pi}{2} \frac{|\epsilon_R|^2}{\alpha}) -$
 2793 1, to first order in $|\epsilon_R|^2/\alpha$. This approximation holds in the limit that higher order
 2794 terms can be neglected, viz. $|\epsilon_R|^2/\alpha \ll 1$.

2795 **9.2 Exercises**

2796 **9.1 Construct Saturne I synchrotron. Spin Resonances**

2797 Solution: page 346

2798 In this exercise, Saturne I synchrotron is modeled in zgoubi, and spin resonances
2799 in a weak focusing gradient synchrotron are studied.

2800 (a) Construct a model of Saturne I 90° cell dipole in the hard-edge model, using
2801 DIPOLE. Use parameters given in Tab. 9.1, and Fig. 9.18 as a guidance. Take an
2802 integration step size in centimeter range - check convergence as you proceed. In
2803 order to allow beam monitoring, split the dipole in two 45° deg halves. It is judicious
2804 (although in no way a necessity) to take $RM=841.93$ cm in DIPOLE.

2805 Find the 6×6 transport matrix of that dipole. MATRIX can be used for that, with
2806 OBJET[KOBJ=5] to define a proper set of initial coordinates.

2807 Check against theory (refer to Sect. 18.2, Eq. 18.31).

2808 (b) Construct a model of Saturne I cell, with origin at the center of the drift. Take
2809 the reference orbit along the arc of nominal radius in the dipoles, 841.93 cm.

2810 Compute the tunes using MATRIX; check their values against theory.

2811 Move the origin along the drift, verify that, while the cell matrix depends on the
2812 origin, its trace does not change.

2813 Produce a scan of the tunes over the field index range $0.5 \leq n \leq 0.757$. RE-
2814 BELOTE can be used to repeatedly change n over that range. Superimpose the
2815 theoretical curves $\nu_x(n)$, $\nu_y(n)$.

2816 Using TWISS and OBJET[KOBJ=5], produce the periodic beam matrix of the
2817 cell. TWISS causes a print out of both the transport matrix and the periodic beam
2818 matrix: check that these satisfy Eq. 19.14.

2819 (c) Launch 60 particles evenly distributed on a common paraxial horizontal
2820 Courant-Snyder invariant (vertical motion is taken null). Store particle data along
2821 the ring in zgoubi.plt, using DIPOLE[IL=2] and DRIFT[split,N=20,IL=2]. Use these
2822 to produce a graph of $x^2(s) / \varepsilon_x / \pi$.

2823 From this graph, get the value of the betatron function β_x at the ends of the cell,
2824 compare with TWISS outcomes. Find the minimum and maximum values of the
2825 beta functions, and their azimuth $s(\min[\beta_x])$, $s(\max[\beta_x])$. Check the latter against
2826 theory.

2827 Repeat for the vertical motion, taking $\varepsilon_x = 0$, ε_y paraxial.

2828 (d) Answer the previous question using, instead of 60 particles, a single particle
2829 traced over a few tens of turns.

2830 (e) Find the closed orbit for an off-momentum particle. FIT can be used for that.
2831 From the raytracing outcomes, produce a graph of the dispersion function $D_x(s)$.

(f) Justify considering the betatron oscillation as sinusoidal, namely,

$$y(\theta) = A \cos(\nu_y \theta + \phi)$$

2832 wherein $\theta = s/R$, $R = \oint ds / 2\pi$.

2833 Find the value of the horizontal and vertical betatron functions, resulting from
2834 that approximation. Compare with the betatron functions obtained in (b).

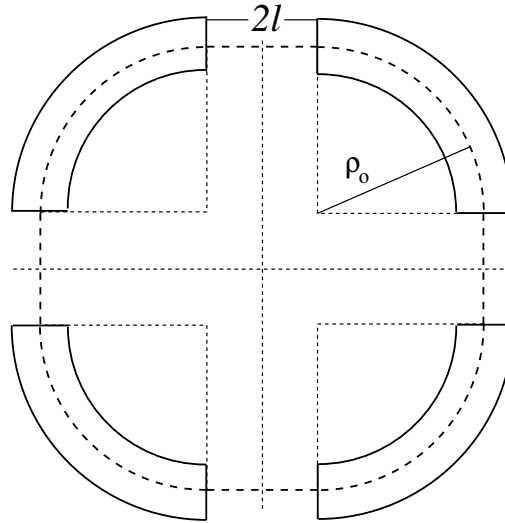


Fig. 9.18 A schematic layout of Saturne I, a $2\pi/4$ axial symmetry structure, comprised of 4 radial field index 90 deg dipoles and 4 drift spaces. The cell in the simulation exercises is taken as a $\pi/4$ quadrant: l-drift/90°-dipole/l-drift

Table 9.1 Parameters of Saturne 1 weak focusing synchrotron [21]. ρ_0 denotes the reference bending radius in the dipole; the reference orbit, field index, wave numbers, etc., are taken along that radius

Orbit length, C	cm	6890
Average radius, $R = C/2\pi$	cm	1096.58
Straight section length, $2l$	cm	400
Magnetic radius, ρ_0	cm	841.93
R/ρ_0		1.30246
Field index n , nominal value		0.6
Wave numbers, $\nu_x; \nu_y$		0.724; 0.889
Stability limit		$0.5 < n < 0.757$
Injection energy	MeV	3.6
Field at injection	kG	0.0326
Top energy	GeV	2.94
\dot{B}	T/s	1.8
Field at top energy, B_{\max}	kG	14.9
$B_{\max}\rho$	T m	13
Field ramp at injection	kG/s	20
Synchronous energy gain	keV/turn	1.160
RF harmonic		2

2835 (g) Produce an acceleration cycle from 3.6 MeV to 3 GeV, for a few particles
 2836 launched on a common $10^{-4} \pi\text{m}$ initial invariant in each plane. Ignore synchrotron
 2837 motion (CAVITE[I OPT=3] can be used in that case). Take a peak voltage $\hat{V} = 200 \text{ kV}$
 2838 (unrealistic though, as it would result in a nonphysical \dot{B} (Eq. 9.29)) and synchronous
 2839 phase $\phi_s = 150 \text{ deg}$ (justify $\phi_s > \pi/2$).

2840 Check the accuracy of the betatron damping over the acceleration range, compared
 2841 to theory.

2842 How close to symplectic the numerical integration is (it is by definition *not*
 2843 symplectic, being a truncated Taylor series method [22, Eq. 1.2.4]), depends on the
 2844 integration step size, and on the size of the flying mesh in the DIPOLE method [22,
 2845 Fig. 20]; check a possible departure of the betatron damping from theory as a function
 2846 of these parameters.

2847 Produce a graph of the the evolution of the horizontal and vertical wave numbers
 2848 during the acceleration cycle.

2849 (h) Change the peak voltage to $\hat{V} = 20$ kV. Produce a graph of the value of the
 2850 vertical spin component of the particles as a function of $G\gamma$, over the acceleration
 2851 range from 3.6 MeV to 3 GeV. Adding SPNTRK will ensure spin tracking.

2852 Produce a graph of the average value of S_Z over that 200 particle set, as a function
 2853 of $G\gamma$. Indicate on that graph the location of the resonant $G\gamma_R$ values.

2854 (i) Based on the simulation file used in (f), simulate the acceleration of a single
 2855 particle, through the intrinsic resonance $G\gamma_R = 4 - \nu_Z$, from a few thousand turns
 2856 upstream to a few thousand turns downstream.

2857 Perform this resonance crossing for five different values of the particle invariant,
 2858 namely: $\varepsilon_Z/\pi = 2, 10, 20, 40, 200 \mu\text{m}$.

2859 Compute P_f/P_i in each case, check the dependence on ε_Z against theory. Com-
 2860 pute the resonance strength in each case, check the dependence on ε_Z against theory.

2861 Re-do this crossing simulation for a different crossing speed (take for instance
 2862 $\hat{V} = 10$ kV) and a couple of vertical invariant values, compute P_f/P_i so obtained.
 2863 Check the crossing speed dependence of P_f/P_i against theory.

2864 (j) Plot the turn-by-turn vertical spin component motion $S_Z(\text{turn})$ across the
 2865 resonance $G\gamma_R = 4 - \nu_Z$, in a weakly depolarizing case, $P_f \approx P_i$. Show that it
 2866 satisfies Eq. 9.43. Match the data to the latter to get the vertical betatron tune ν_y , and
 2867 the location of the resonance $G\gamma_R$.

2868 (k) Track a few particles at fixed energy, at distances from the resonance $G\gamma_R =$
 2869 $4 - \nu_y$ of up to a $7 \times \varepsilon_R$ (this distance corresponds to 1% depolarization).

2870 Produce on a common graph the spin motion $S_Z(\text{turn})$ for all these particles, as
 2871 observed at some azimuth along the ring.

2872 Produce a graph of $\langle S_y \rangle_{\text{turn}}(\Delta)$ (as in Fig. 9.16).

Produce the vertical betatron tune ν_y , and the location of the resonance $G\gamma_R$,
 obtained from a match of these tracking trials to the theoretical (Eq. 9.41)

$$\langle S_y \rangle(\Delta) = \frac{\Delta}{\sqrt{|\varepsilon_R|^2 + \Delta^2}}$$

2873 9.2 Construct the ZGS synchrotron. Spin Resonances

2874 Solution: page 371

2875 In this exercise, ZGS synchrotron is modeled in zgoubi, and spin resonances in
 2876 this weak focusing zero-gradient synchrotron are studied.

2877 (a) Construct an approximate model of the ZGS synchrotron, using DIPOLE.
 2878 Use Figs. 9.19, 9.20 as a guidance, and parameters given in Tab. 9.2. Assume that
 2879 the reference orbit is the same at all energies, on nominal radius, 2076 cm. It is
 2880 judicious (although in no way an obligation) to take RM=2076 in DIPOLE. (Note

2881 that in reality, unlike the present assumption for this exercise, the reference orbit in
 2882 ZGS would be moved outward during acceleration [23].)

2883 Check the correctness of the model by producing the lattice parameters of the
 2884 ring. TWISS can be used for that. Compare with the lattice parameters given in
 2885 Tab. 9.2.

2886 (b) Produce a graph of the betatron functions along the ZGS cell. Provide checks
 2887 of the correctness of the computation.

2888 Check the theoretical periodic dispersion (Eq. 9.27) against the radial distance
 2889 between on- and off-momentum closed orbits obtained from raytracing. Provide a
 2890 plot of the dispersion function.

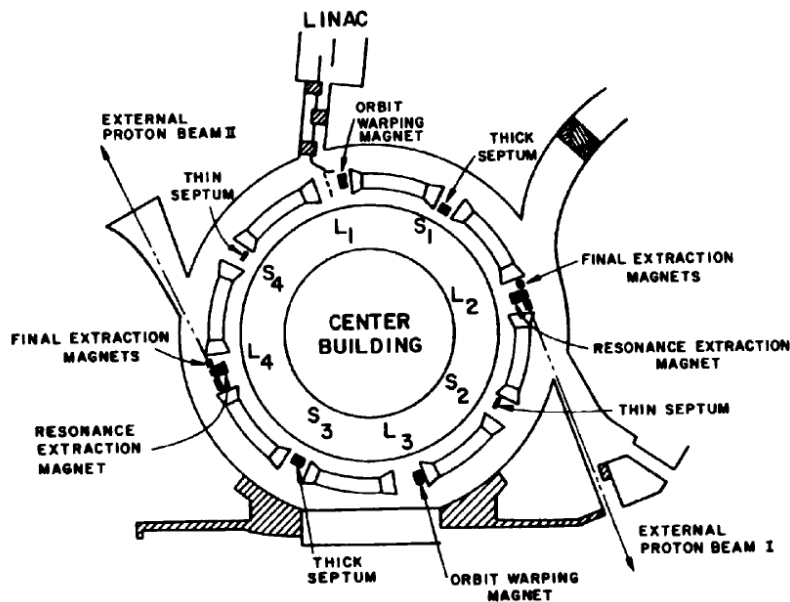


Fig. 9.19 A schematic layout of the ZGS [?], a $\pi/2$ -periodic structure, comprised of 8 zero-index dipoles, 4 long and 4 short straight sections

2891 (c) Additional verifications regarding the model.

2892 Produce a graph of the field $B(s)$

2893 - along the on-momentum closed orbit, and along off-momentum chromatic closed
 2894 orbits, across a cell;

2895 - along orbits at large horizontal excursion;

2896 - along orbits at large vertical excursion.

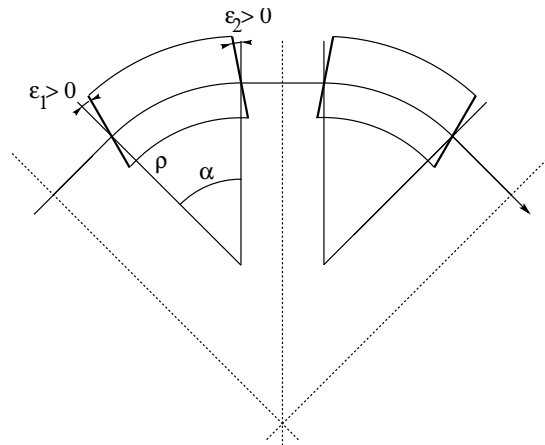


Fig. 9.20 A sketch of ZGS cell layout. In defining the entrance and exit faces (EFBs) of the magnet, beam goes from left to right. Wedge angles at the long straight sections (ε_1) and at the short straight sections (ε_2) are different

2897 For all these cases, verify qualitatively, from the graphs, that $B(s)$ appears as
2898 expected.

(d) Justify considering the betatron oscillation as sinusoidal, namely,

$$y(\theta) = A \cos(\nu_y \theta + \phi)$$

2899 wherein $\theta = s/R$, $R = \oint ds/2\pi$.

2900 Find the value of the horizontal and vertical betatron functions, resulting from
2901 that approximation. Compare with the betatron functions obtained in (b).

2902 (e) Produce an acceleration cycle from 50 MeV to 17 GeV about, for a few particles
2903 launched on the a common $10^{-5} \pi$ m vertical initial invariant, with small horizontal
2904 invariant. Ignore synchrotron motion (CAVITE[IOPT=3] can be used in that case).
2905 Take a peak voltage $\hat{V} = 200$ kV (this is unrealistic but yields 10 times faster
2906 computing than the actual $\hat{V} = 20$ kV, Tab. 9.2) and synchronous phase $\phi_s = 150$ deg
2907 (justify $\phi_s > \pi/2$). Add spin, using SPNTRK, in view of the next question, (f).

2908 Check the accuracy of the betatron damping over the acceleration range, compared
2909 to theory. How close to symplectic the numerical integration is (it is by definition
2910 *not* symplectic), depends on the integration step size, and on the size of the flying
2911 mesh in the DIPOLE method [22, Fig. 20]; check a possible departure of the betatron
2912 damping from theory as a function of these parameters.

2913 Produce a graph of the the evolution of the horizontal and vertical wave numbers
2914 during the acceleration cycle.

Table 9.2 Parameters of the ZGS weak focusing synchrotron after Refs. [23, 24] [?, pp.288-294,p. 716] (2nd column, when they are known) and in the present simplified model and numerical simulations (3rd column). Note that the actual orbit is skewed (moves) during ZGS acceleration cycle, tunes change as well - this is not the case in the present modeling

		From Refs. [23, 24]	Simplified model
Injection energy	MeV		50
Top energy	GeV		12.5
$G\gamma$ span		1.888387 - 25.67781	
Length of central orbit	m	171.8	170.90457
Length of straight sections, total	m	41.45	40.44
<i>Lattice</i>			
Wave numbers $\nu_x; \nu_y$		0.82; 0.79	0.849; 0.771
Max. $\beta_x; \beta_y$	m		32.5; 37.1
<i>Magnet</i>			
Length	m	16.3	16.30486 (magnetic)
Magnetic radius	m	21.716	20.76
Field min.; max.	kG	0.482; 21.5	0.4986; 21.54
Field index			0
Yoke angular extent	deg	43.02590	45
Wedge angle	deg	≈ 10	13 and 8
<i>RF</i>			
Rev. frequency	MHz	0.55 - 1.75	0.551 - 1.751
RF harmonic $h = \omega_{rf} / \omega_{rev}$			8
Peak voltage	kV	20	200
B-dot, nominal/max.	T/s	2.15/2.6	
Energy gain, nominal/max.	keV/turn	8.3/10	100
Synchronous phase, nominal	deg		150
<i>Beam</i>			
$\varepsilon_x; \varepsilon_y$ (at injection)	$\pi \mu\text{m}$		25; 150
Momentum spread, rms			3×10^{-4}
Polarization at injection	%	>75	100
Radial width of beam (90%), at inj.	inch	2.5	$\sqrt{\beta_x \varepsilon_x / \pi} = 1.1$

- 2915 (f) Using the raytracing material developed in (e): produce a graph of the vertical
 2916 spin component of the particles, and the average value over that 200 particle set, as
 2917 a function of $G\gamma$. Indicate on that graph the location of the resonant $G\gamma_R$ values.

- 2918 (g) Based on the simulation file used in (f), simulate the acceleration of a single
 2919 particle, through one particular intrinsic resonance, from a few thousand turns
 2920 upstream to a few thousand turns downstream.
 2921 Perform this resonance crossing for different values of the particle invariant.
 2922 Determine the dependence of final/initial vertical spin component value, on the
 2923 invariant value; check against theory.
 2924 Re-do this crossing simulation for a different crossing speed. Check the crossing
 2925 speed dependence of final/initial vertical spin component so obtained, against theory.
- 2926 (h) Introduce a vertical orbit defect in the ZGS ring.
 2927 Find the closed orbit.
 2928 Accelerate a particle launched on that closed orbit, from 50 MeV to 17 GeV about,
 2929 produce a graph of the vertical spin component.
 2930 Select one particular resonance, reproduce the two methods of (g) to check the
 2931 location of the resonance at $G\gamma_R = \text{integer}$, and to find its strength.

2932 References

- 2933 1. Veksler, V.: A new method of acceleration of relativistic particles. J. of Phys. USSR 9 153-158
 2934 (1945)
 2935 2. McMillan, E. M.: The Synchrotron. Phys. Rev. 68 143-144 (1945)
 2936 3. Goward, F. K., and Barnes, D. E.: Experimental 8 MeV synchrotron for electron acceleration.
 2937 Nature 158, 413 (1946)
 2938 4. Richardson, J.R., et al.: Frequency Modulated Cyclotron. Phys. Rev. 69: 669 (1946)
 2939 5. Kerst, D. W.: The Acceleration of Electrons by Magnetic Induction.. Phys. Rev., 60, 47-53
 2940 (1941)
 2941 6. Photo saturne I. ***** TB completed **** Archives historiques CEA. Copyright
 2942 CEA/Service de documentation - FAR_SA_N_00248
 2943 7. Photo tranche dipole. Credit: CEA Saclay. ***** TB completed *****
 2944 Archives historiques CEA. Copyright CEA/Service de documentation - FAR_SA_N_02826
 2945 8. Ratner, L.G. and Khoe, T.K.: Acceleration of Polarized Protons in the Zero Gradient Syn-
 2946 chrotron. Procs. PAC 1973 Conference, Washington (1973).
 2947 http://accelconf.web.cern.ch/p73/PDF/PAC1973_0217.PDF
 2948 9. Vostrikov, V.A., et al.: Novel approach to design of the compact proton synchrotron magnetic
 2949 lattice. 26th Russian Particle Accelerator Conference RUPAC2018, Protvino, Russia (2018).
 2950 <https://accelconf.web.cern.ch/rupac2018/papers/tupsa17.pdf>.
 2951 Fig. 9.3: Copyrights under license CC-BY-3.0, <https://creativecommons.org/licenses/by/3.0/>;
 2952 no change to the material
 2953 10. Suddeth, D.E., et als.: Pole face winding equipment for eddy current correction at the Zero
 2954 Gradient Synchrotron. Procs. PAC 1973 Conference, Washington (1973).
 2955 http://accelconf.web.cern.ch/p73/PDF/PAC1973_0397.PDF
 2956 11. Rauchas, A.V. and Wright, A.J.: Betatron tune profile control in the Zero Gradient Synchrotron
 2957 (ZGS) using the main magnet pole face windings. Procs. PAC1977 conference, IEEE Trans.
 2958 on Nucl. Science, VoL.NS-24, No.3, June 1977
 2959 12. Floquet, G.: Sur les équations différentielles linéaires à coefficients périodiques. Annales
 2960 scientifiques de l'E.N.S. 2e série, tome 12 (1883), p. 47-88.
 2961 http://www.numdam.org/item?id=ASENS_1883_2_12_47_0
 2962 13. Leleux, G.: Accélérateurs Circulaires. Lecture Notes, INSTN, CEA Saclay (1978)

- 2963 14. Bohm, D. and Foldy, L.: Theory of the Synchro-Cyclotron. *Phy. Rev.* 72, 649-661 (1947).
- 2964 15. Cohen, D. : Feasibility of Accelerating Polarized Protons with the Argonne ZGS. *Review of*
2965 *Scientific Instruments* 33, 161 (1962).// <https://doi.org/10.1063/1.1746524>
- 2966 16. Cho, Y., et als.: Effects of depolarizing resonances on a circulating beam of polarized protons
2967 during or storage in a synchrotron. *IEEE Trans. Nuclear Science*, Vol.NS-24, No.3, June 1977
- 2968 17. Parker, E.F.: High Energy Polarized Deuterons at the Argonne National Laboratory Zero
2969 Gradient Synchrotron. *IEEE Transactions on Nuclear Science*, Vol. NS-26, No. 3, June 1979,
2970 pp 3200-3202
- 2971 18. Lee, S.Y.: *Spin Dynamics and Snakes in Synchrotrons*. World Scientific, 1997
- 2972 19. Froissart, M. and Stora, R.: Dépolarisation d'un faisceau de protons polarisés dans un syn-
2973 chrotron. *Nucl. Inst. Meth.* 7 (1960) 297.
- 2974 20. Leleux, G.: Traversée des résonances de dépolarisation. Rapport Interne LNS/GT-91-15,
2975 Saturne, Groupe Théorie, CEA Saclay (février 1991)
- 2976 21. Bruck H., Debraine P., Levy-Mandel R., Lutz J., Podliasky I., Prevot F., Taieb J., Winter S.D.,
2977 Maillet R., Caractéristiques principales du Synchrotron à Protons de Saclay et résultats obtenus
2978 lors de la mise en route, rapport CEA no.93, CEN-Saclay, 1958.
- 2979 22. Méot, F.: Zgoubi Users' Guide.
2980 <https://www.osti.gov/biblio/1062013-zgoubi-users-guide> Sourceforge latest version:
2981 <https://sourceforge.net/p/zgoubi/code/HEAD/tree/trunk/guide/Zgoubi.pdf>
- 2982 23. Foss, M.H., et al.: The Argonne ZGS Magnet. *IEEE* 1965, pp. 377-382, June 1965
- 2983 24. Klaisner, L.A., et al.: *IEEE* 1965, pp. 133-137, June 1965